

Supplemental Information

Large Scale 2D/3D Hybrids based on Gallium Nitride and Transition Metal Dichalcogenides

Kehao Zhang^{1,2}, Bhakti Jariwala¹, Jun Li³, Natalie C. Briggs¹, Baoming Wang^{2,4}, Dmitry Ruzmetov^{2,5}, Robert A. Burke^{2,5,7}, Jordan O. Lerach⁶, Tony G. Ivanov^{2,5}, Md Haque^{2,4}, Randall M. Feenstra³, and Joshua A. Robinson^{1,2}

1. Department of Materials Science and Engineering & Center for Two-Dimensional and Layered Materials, The Pennsylvania State University, University Park, Pennsylvania 16802, United States
2. Center for Atomically Thin Multifunctional Coating, University Park, Pennsylvania 16802, United States
3. Department of Physics, Carnegie Mellon University, Pittsburgh, Pennsylvania 15213, United States
4. Department of Mechanical and Nuclear Engineering, The Pennsylvania State University, University Park 16802, United States
5. Sensors and Electron Devices Directorate, U.S. Army Research Laboratory, Adelphi, Maryland 20783, United States
6. Materials Characterization Laboratory, The Pennsylvania State University, University Park 16802, United States
7. General Technical Services, LLC, Wall, New Jersey 07727, United States

Thickness controlled synthesis of 2D materials

MoS₂: Monolayer (1L) to few layer (FL) MoS₂ is grown using metalorganic precursors in a hot-wall tube furnace. Molybdenum hexacarbonyl (Mo(CO)₆) and diethyl sulfide (DES) precursors are sealed in two individual bubblers as shown in Fig. S1a. The GaN samples are loaded into the center of the furnace with 1mg of NaCl powder upstream. Before the growth, the chamber is annealed in vacuum (18 mTorr) at 300°C for 5 mins to remove moisture and contaminants from the system, and then the chamber pressure is increased to 10 Torr with 565 sccm Ar as the carrier gas. At the beginning of the growth step, a two-minute nucleation step is carried out with 2 sccm H₂ flowing through the Mo(CO)₆ bubbler and 45 sccm H₂ flowing through the DES bubbler. Afterwards, the H₂ flow rate for Mo(CO)₆ is increased to 5sccm. The entire growth takes 30 mins, 60 mins and 120 mins to grow 1L, 2L and ~5L MoS₂ on pGaN, respectively.

NaCl has become a popular addition for MOCVD growth of MoS₂ in order to eliminate moisture in the system and suppress the nucleation.^{1,2} We have also found that NaCl is effective in removing the carbon residuals caused by the metal organic precursors. Nanocrystalline MoS₂ flakes are observed by AFM (Fig. S1b-c) when the NaCl is utilized, while a uniform layer with 0.3 nm thickness is observed underneath the triangular MoS₂ film when NaCl is not present (Fig. S1d-e). Raman spectra shown in Fig. S1e suggests that although MoS₂ can be synthesized either with or without NaCl, growth without NaCl results in a significant amount of carbon due to the presence of a thin layer of carbon being present underneath the MoS₂. More theoretical calculations are needed to understand the reaction between the NaCl and the precursors.

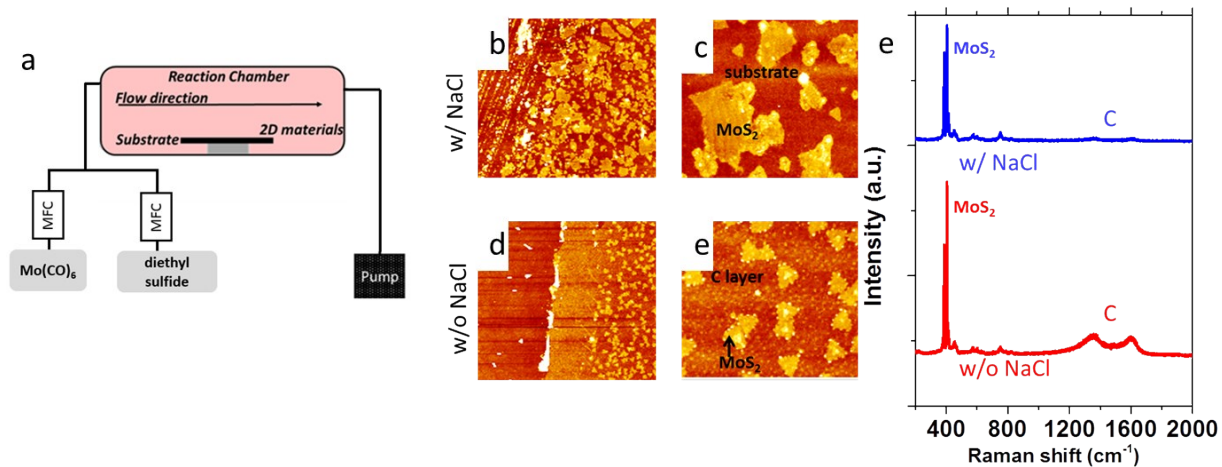


Figure S1-The growth setup and fundamental characterization: a. schematic of the MOCVD reactor for MoS₂ growth; b-c. large scale (10um) and small scale (2um) AFM scans of MoS₂ grown with NaCl; d-e. large scale (10um) and small scale (2um) AFM scans of MoS₂ grown without NaCl. A clear carbon film is observed after growth without NaCl; e. Raman spectra of the MoS₂ grown with (blue) and without NaCl (red), clearly demonstration the presence of carbon peaks when growth is carried out without NaCl present.

WSe₂: Growing 2D vdW layered material on 3D substrates is not the same as traditional epitaxy due to the absence of dangling bonds on the surface. Here, we have shown the epitaxial growth of WSe₂ on n-GaN with uniform coverage without any degradation of the GaN substrate. Growths were performed in a vertical cold wall MOCVD reactor³ near atmospheric pressure (700 torr) using H₂ as a carrier gas using the growth profile as shown in Fig. S2. The precursors, W(CO)₆ and H₂Se, were introduced to the chamber simultaneously just after temperature reached 650°C in order to avoid roughening the GaN surface due to the possibility of degradation under a H₂ environment. An epitaxial 2L WSe₂ film was obtained in a 30-minute growth for a partial pressure of 5.8x10⁻⁴ Torr for W(CO)₆ and 11 Torr for H₂Se. A 5 min anneal under a H₂Se environment was performed at the end of growth process in order to reduce chalcogenide based defects in the film which have been observed in a previous study (Science paper). A sharp and abrupt interface at the GaN surface (based on cross-sectional TEM) presents a controlled layer-by-layer growth with vdW epitaxy of the WSe₂. We believe that passivation of the surface dangling bonds on a 3D substrate is key to achieving vdW epitaxial growth of 2D layers on ordinary 3D substrates.

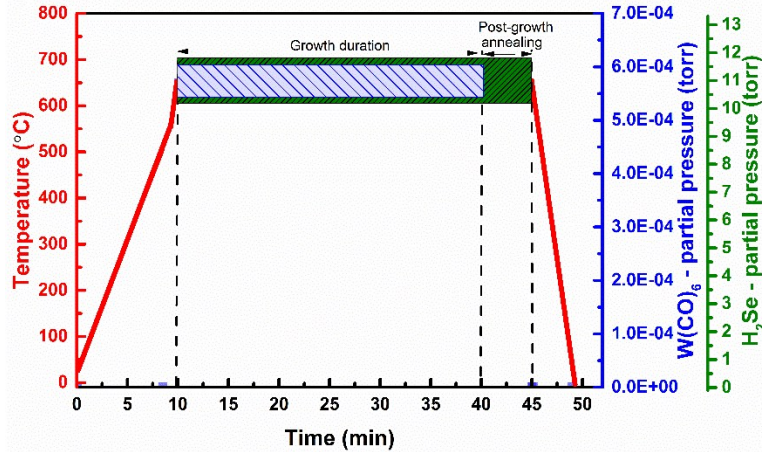


Figure S2-The growth temperature/flow/pressure profile of MOCVD growth of WSe₂ on n-GaN.

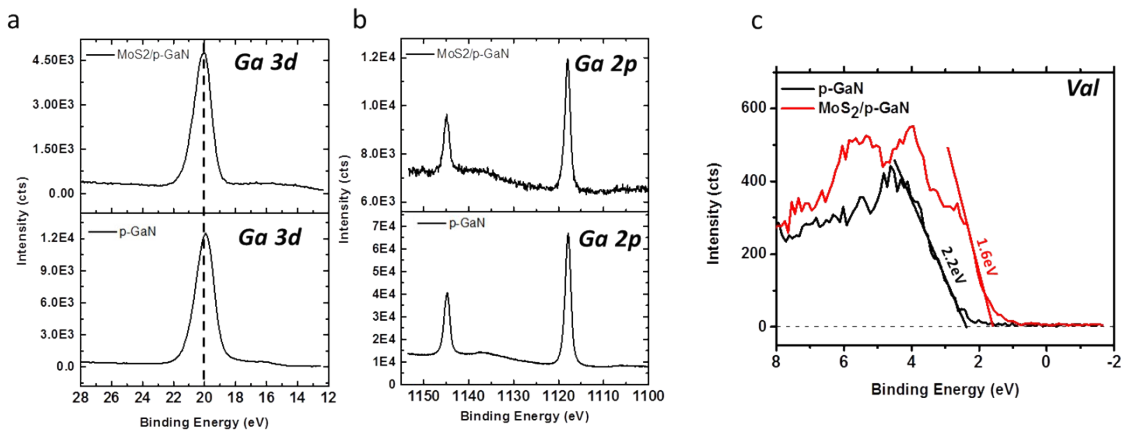
Raman characterization procedure

Room temperature Raman characterizations were carried out with a Horiba Scientific confocal Raman system with 488nm laser at 1.1 mW. The accumulation time was 10 s and the spectra were accumulated twice to increase the signal/noise ratio. All the Raman spectra shown in this study were taken under exactly identical condition to ensure a fair comparison.

XPS experimental procedure

X-ray photoelectron spectroscopy (XPS) measurements were carried out with a Physical Electronics Versa Probe II equipped with a monochromatic Al K_α X-ray source ($h\nu=1486.7$ eV) and a concentric hemispherical analyzer. High resolution spectra were obtained over an analysis area of 200 μm at a pass energy of 23.5 eV and resolution of 0.1 eV. The resulting spectra were charge referenced to adventitious carbon corresponding to carbon 1s at 284.8 eV.

Supplemental XPS study



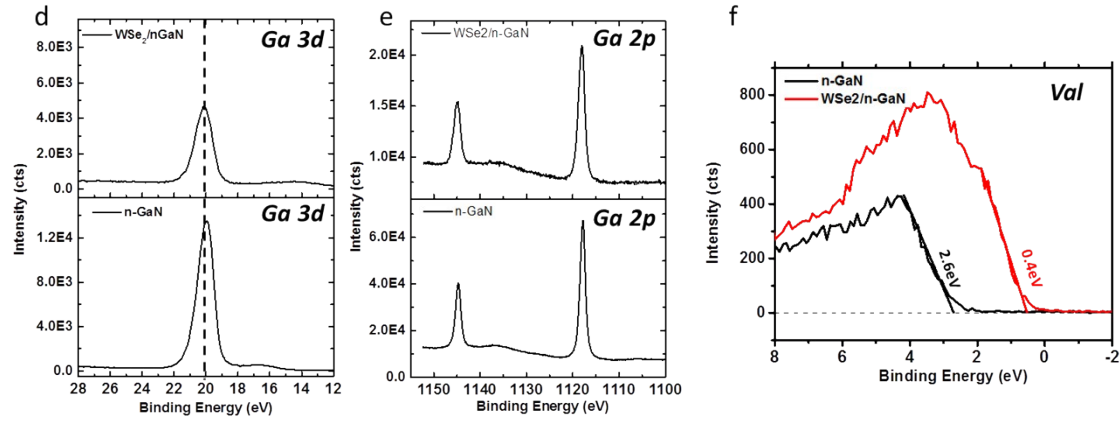


Figure S3- XPS characterization of TMD/GaN heterostructures. a-b. XPS of p-GaN before and after the MoS₂ growth. For the Ga 3d and Ga 2p peaks, there is no obvious evidence indicating a structural change after the MoS₂ growth; c. The valence band edge of the MoS₂/pGaN heterostructure and bare pGaN. The valence band maximum is 1.4 eV and 2.2 eV below the Fermi level for MoS₂ and pGaN respectively, indicating that the MoS₂ is n-type and GaN is n-type on the surface due to surface passivation but that the bulk properties exhibit p-type characteristics; d-e. XPS of n-GaN before and after the WSe₂ growth. For the Ga 3d and Ga 2p peaks, there is no obvious evidence indicating a structural change after the growth; f. The valence band maximum is 0.4eV and 2.6eV below the Fermi level for WSe₂ and nGaN respectively, indicating that the WSe₂ is p-type and GaN is n-type.

Electrical Analysis of the heterostructures

The vertical transport properties are characterized by conductive AFM. A Bruker Icon II and SCM-PIT-V2 Pt/Ir tip are employed in this experiment. Figure S4a shows the I-V curve of pGaN, 1L MoS₂/pGaN and FL MoS₂/pGaN. Rectifying behavior is observed on p-GaN under forward bias from the sample due to the well-known Schottky barrier between pGaN and Pt.^{3,4} Interestingly, 1L MoS₂/pGaN shows a very similar rectifying behavior as pGaN, while a relatively high leakage current is observed on FL MoS₂/pGaN. To probe this characteristic, the I-V curve is replotted based on the Fowler-Nordheim (F-N) equations (Eq. S1) to test the linearity of the data:

$$\ln\left(\frac{I}{V^2}\right) \propto \ln\left(\frac{1}{V}\right) - \frac{4\pi d\sqrt{2m^* \Phi_B}}{h} \quad (\text{Eq. S1 a: Direct tunneling})$$

$$\ln\left(\frac{I}{V^2}\right) \propto -\left(\frac{1}{V}\right) \frac{8\pi d\sqrt{2m^* \Phi_B^3}}{3hq} \quad (\text{Eq. S1 b: F-N tunneling})$$

where Φ_B is Schottky barrier height, m^* is the effective mass of electrons in the MoS₂ channel, q is the electron charge, h is the Planck's constant, and d is the width of the barrier. The plot of $\ln(I/V^2)$ vs $(1/V)$ is shown in Fig. S4b. It is clear that $1/V$ is linear with $\ln(I/V^2)$ at higher voltage logarithms and lower voltages for 1L MoS₂, indicating that direct tunneling is dominant at lower voltages, and F-N is dominant at higher voltages. In contrast, there is no clear linear or logarithmic relationship between $\ln(I/V^2)$ vs $(1/V)$ for FL MoS₂, suggesting the tunneling is suppressed and other mechanisms should be responsible

for the vertical transport.⁵ The tunneling-dominated I-V curve is also valid in the WSe₂ case (Fig. S4c-d). For atomically thin films, the vertical charge distribution is different from conventional 3D junctions, resulting in a thickness dependent unipolar/ambipolar 2D p-n diode.⁶

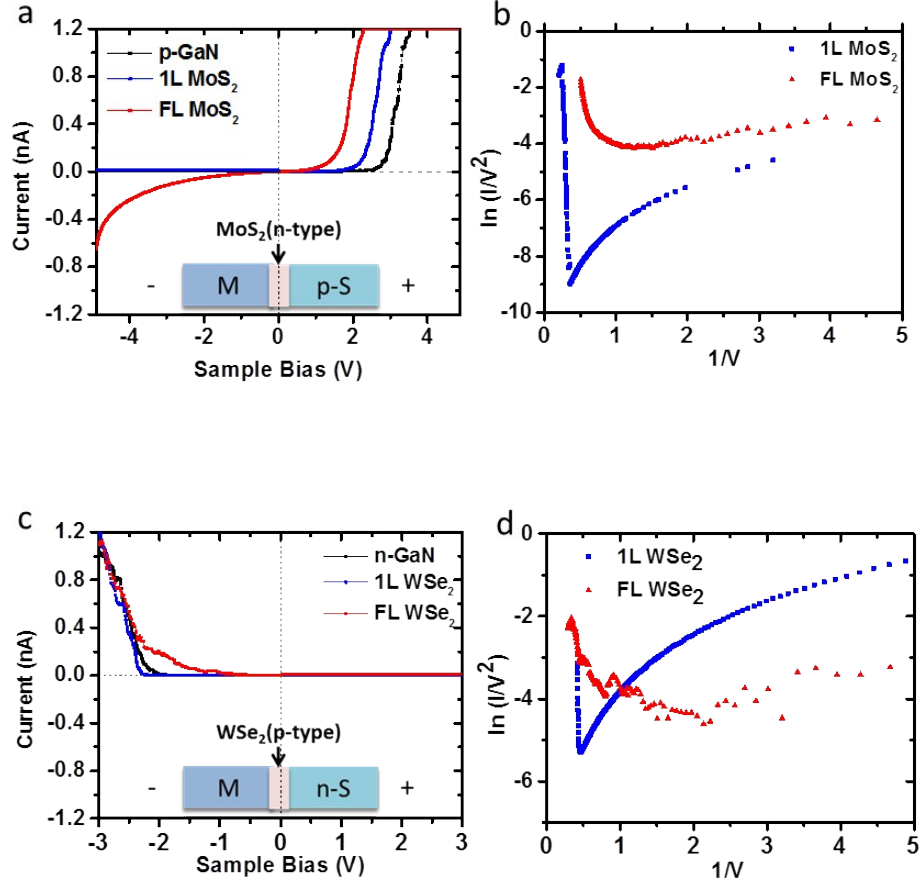


Figure S4-Electrical analysis of thickness dependent TMD/GaN heterostructures. a-b. Linear and Fowler-Nordheim plot of 1L and FL MoS₂ on p-GaN; c-d. Linear and Fowler-Nordheim plot of 1L and FL WSe₂ on n-GaN. A distinct direct tunneling difference is observed for 1L TMD/GaN structures.

Here we calculate the depletion width of tip/GaN, tip/MoS₂, based on the classic solution of Poisson equation (Equation S2 a) in order to further understand the thickness-dependent vertical transport. Note that the built-in potential for tip/WSe₂ is <0 in theory, which indicates the contact is Ohmic, so the depletion width of tip/WSe₂ is not shown in table S1.

$$x_d = \sqrt{\frac{2\epsilon_s(\Phi_i - V_a)}{qN_d}} \quad (\text{Eq. S2 a: depletion width})$$

Where ϵ_s is the relative permittivity of the semiconductor, Φ_i is the built in potential of the metal-insulating junction that can be calculated by equation S2 b-c, q is the charge of the electron, and N_d is the carrier concentration of the semiconductor.

$$\Phi_i = \Phi_M - \chi - \frac{E_C - E_{F,n}}{q} \quad (\text{Eq. S2 b: built-in potential})$$

$$\Phi_i = \chi + \frac{E_C - E_{F,p}}{q} - \Phi_M \quad (\text{Eq. S2 c: built-in potential})$$

Where Φ_M is the work function of metal contact, χ is the electron affinity of the semiconductor, E_C and E_F is the conduction band energy and Fermi level energy, respectively. The used parameter and calculated results are shown in Table S1. The depletion width is estimated to be equal to ~5-6 layers of MoS₂, which agrees our experimental results. Further advanced calculation such as DFT should be considered for a more accurate estimation of the depletion width.

Table S1: The Calculated Schottky barrier depletion width

System	WF Metal	EA Semi	Ef	Vbi	Nd	ϵ_s	X_d
Tip/pGaN	5.4eV	4.2eV ⁷	7.0eV ⁸	1.6eV	10 ¹⁷	9.8 ⁹	131.7nm
Tip/nGaN	5.4eV	4.1eV ¹⁰	4.5eV	0.9eV	10 ¹⁸	9.8 ⁹	31.23nm
Tip/MoS ₂	5.4eV	4.2eV ¹¹	4.5eV	1.0eV/0.25eV (Fermi Pining)	10 ¹⁹	4.0	6.65nm/3.33nm (Fermi Pining)

The 2D/3D p-n diode is analyzed by equation S3:¹²

$$I = I_s \left[\exp\left(\frac{qV}{nkT}\right) - 1 \right] \quad \text{Equation S3}$$

where I_s is reverse saturation current, V is the applied voltage, n is the ideality factor, k is the Boltzmann constant, and T is the temperature (300K in our case). The log scale of the p-n diode established by FL TMDs/GaN is shown in Figure S5.

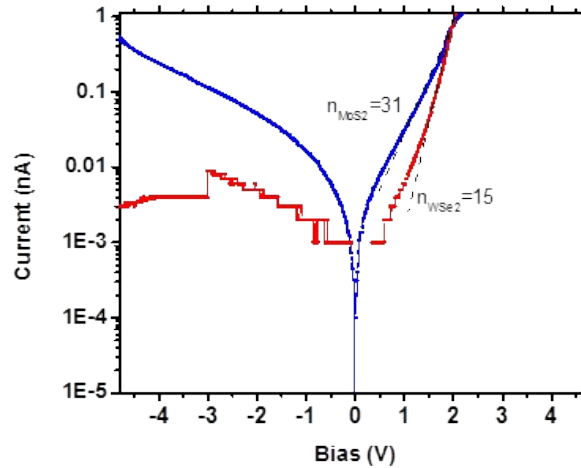


Figure S5-The logarithm scale of p-n diode based on WSe₂/n-GaN (red) and MoS₂/p-GaN (blue), and the ideality is extracted by the linear fitting and equation S4.

It is observed that the ideality factors for both heterostructures are larger than a conventional 3D p-n diode. We attribute this to: a) the measurement technique. Conductive AFM is a simple and convenient technique to acquire electrical data in nanoscale range. However, the poor contact at the tip/sample and sample/stage interface can severely reduce the performance of the materials. Therefore, a device with improved contact will be fabricated in the future. B) the presence of a Schottky barrier. For the aforementioned heterostructures, the addition of the tip/semiconductor Schottky barrier can significantly increase the ideality factor, which has been observed before.¹³ Therefore, we believe that the measured electrical properties here are under estimated and can be improved with state-of-art fabrication techniques.

Kelvin Probe Force Microscope (KPFM) Characterization

Kelvin Probe Force Microscope is conducted on a Bruker Icon II with a PFQNE-Al tip. Before the measurements on the TMD/GaN samples, the work function of the tip is calibrated with a freshly exfoliated standard highly oriented pyrolytic graphite (HOPG) sample ($\Phi=4.6\text{eV}$). The work function of the tip is calculated by equation S4:¹⁴

$$V_{CPD} = \frac{\Phi_{tip} - \Phi_{sample}}{-e} \quad (\text{Equation S4})$$

The topography and potential maps are shown in Fig. S6a-b respectively. The potential curve is shown in Fig. S6c. The average potential (V_{CPD}) is measured as 425 mV, therefore the work function of the tip is 4.18 eV.

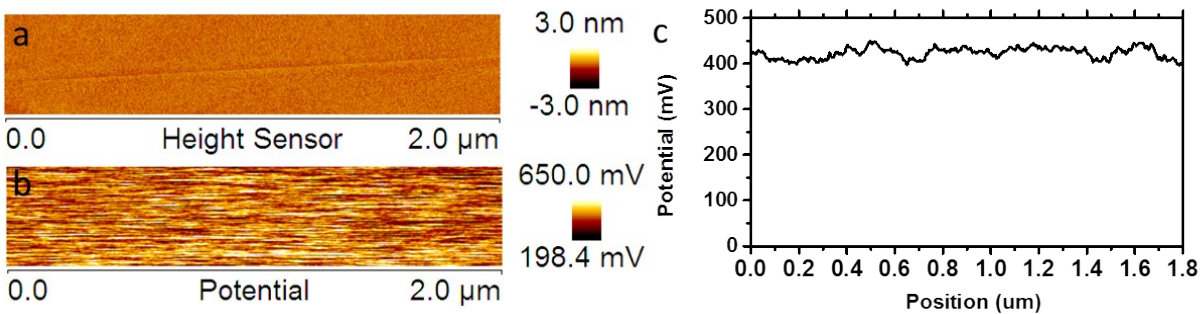


Figure S6- KPFM tip calibration on HOPG. a. The topography of the HOPG sample; b. The potential map of the HOPG sample; c. The averaged potential curve of the HOPG.

Determination of Band offset

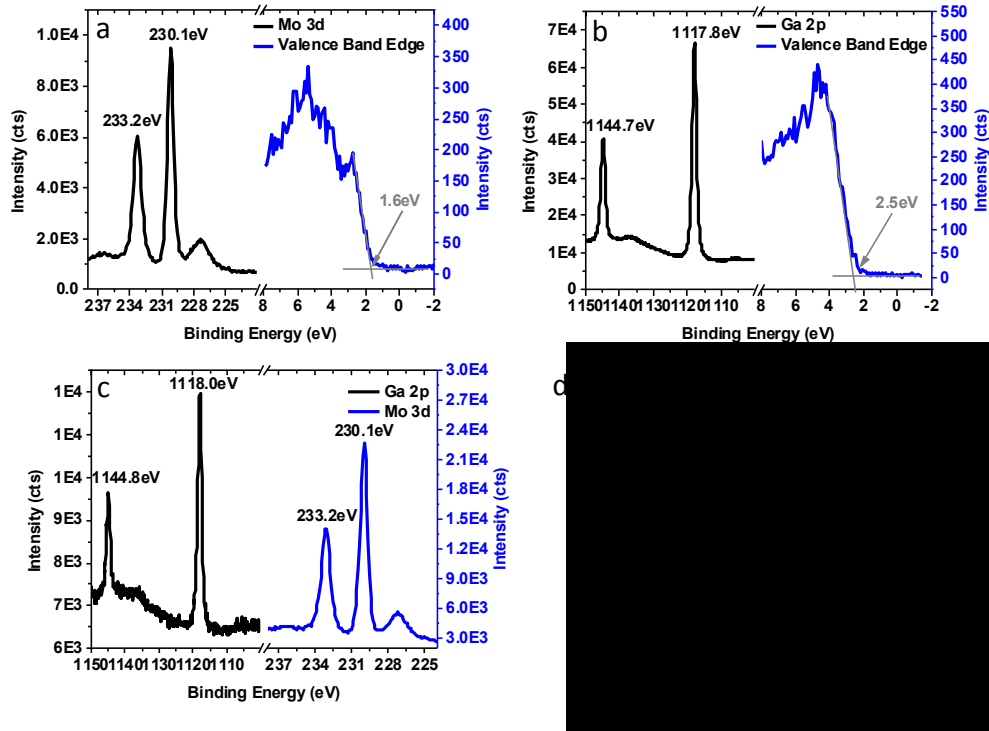
To determine the band offset of FL MoS₂/p-GaN and FL WSe₂/n-GaN heterostructures, the core level of the TMD metals (Mo 3d, W 4f) and the core level of Ga (2p) are measured together with valence band maxima (VBM) by XPS. The core level (Ga 2p) and VBM of bare p/n GaN substrates are also measured by XPS. The spectra and labelled peak positions are shown in Figure S7a-c (MoS₂) and e-g (WSe₂). It is noted that the VBM of the p-GaN is 2.5eV and it could be due to surface contamination and band bending.^{15,16}

The band offset of FL MoS₂/p-GaN and FL WSe₂/n-GaN heterostructures are calculated by equation S5 and S6,^{17,18} respectively:

$$\Delta Ev = \frac{\Delta E_{Mo3d_5}^{MoS_2} - VBM}{2} + \frac{\Delta E_{Ga2p_3 - Mo3d_5}^{GaN/MoS_2}}{2} - \frac{\Delta E_{Ga2p_3}^{GaN} - VBM}{2} \quad (\text{Equation S5})$$

$$\Delta Ev = \frac{\Delta E_{W4f_7}^{WSe_2} - VBM}{2} + \frac{\Delta E_{Ga2p_3 - W4f_7}^{GaN/WSe_2}}{2} - \frac{\Delta E_{Ga2p_3}^{GaN} - VBM}{2} \quad (\text{Equation S6})$$

The band offsets are shown in Fig. S7d and h. It is clear that the FL MoS₂/p-GaN exhibits a type I band alignment due to a reduction in the band gap with an increase in the MoS₂ thickness compared to the reported alignment.¹⁷ However, the WSe₂/n-GaN shows type II band alignment, agreeing with another report.¹⁸



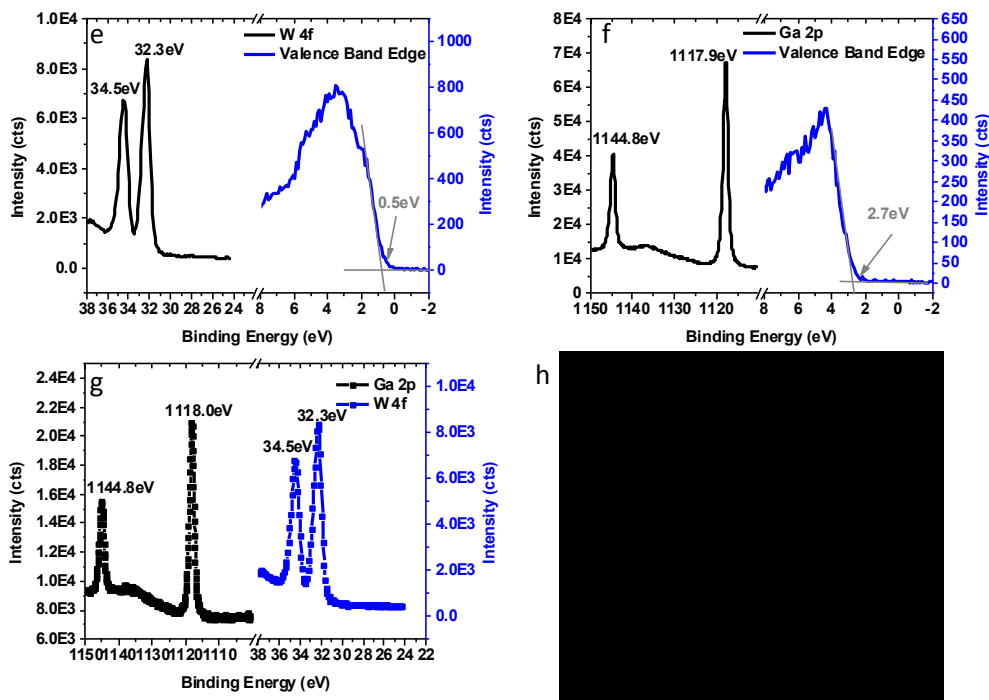


Figure S7- Band offset determination of 2D/3D hybrid by XPS. a. XPS spectra of Mo core level and valence band maxima of MoS₂/p-GaN; b. XPS spectra of Ga core level and valence band maxima of bare p-GaN; c. XPS spectra of Mo and Ga core levels of MoS₂/p-GaN; d. The calculated band offset and band alignment of MoS₂/p-GaN; e. XPS spectra of W core level and valence band maxima of WSe₂/n-GaN; f. XPS spectra of Ga core level and valence band maxima of bare n-GaN; g. XPS spectra of W and Ga core levels of WSe₂/p-GaN; h. The calculated band offset and band alignment of WSe₂/n-GaN.

Low-energy Electron Microscopy (LEEM) characterization

The morphology and variation of the surface work function of TMD/GaN samples is studied in an Elmitec LEEM III instrument. In the principal mode of LEEM, a monochromatic beam of electrons is directed at normal incidence towards the sample surface. Depending on the beam energy and surface states of the sample, a certain number of electrons are reflected back, and these are refocused into an image of the surface using a series of electromagnetic lenses. The beam energy is determined by the bias voltage applied between the sample surface and the electron gun. By taking LEEM images of the surface for a sequence of bias voltages, reflectivity spectra (LEER) can be obtained for each point on the surface. Different domains on the surface can be identified both on the basis of differing contrast in the images and from their reflectivity spectra. We then use the method described in our prior work¹⁹ to extract work function variations of the surface.

Cross-sectional TEM characterization procedure

The cross-section sample was prepared using a focused ion beam (FEI Helios NanoLab 660) and is then examined in a FEI Talos F200X transmission electron microscope (TEM) with an acceleration voltage of 200 kV. The nanostructures are imaged using the bright field high resolution transmission electron

microscope (HRTEM) technique, and the chemical components are analyzed using an integrated SuperX EDS on the Talos instrument under the scanning transmission electron microscope (STEM) mode.

TOF-SIMS Depth Profile

TOF-SIMS depth profiles were collected on a Physical Electronics (Chanhassen, MN, USA) NanoTOF II instrument. Spectral data were collected using a 30 kV Bi liquid metal ion gun selected for the Bi_3^+ ion. Positive ion data was collected over an area of $100 \times 100 \mu\text{m}^2$ with a fluence of 2.5×10^{11} ions/ cm^2 per analysis cycle. Subsequent sputter cycles were generated with a 3 kV Ar^+ ion gun with a sputter fluence of 1.25×10^{14} ions/ cm^2 over an area of $800 \times 800 \mu\text{m}^2$. The TOF-SIMS depth profile of the $\text{MoS}_2/\text{WSe}_2/\text{n-GaN}$ heterostructure is shown in Fig. S8. The elemental map shows a clear difference from Mo to W after three cycles, and it is confirmed by the TOF-SIMS depth profile.

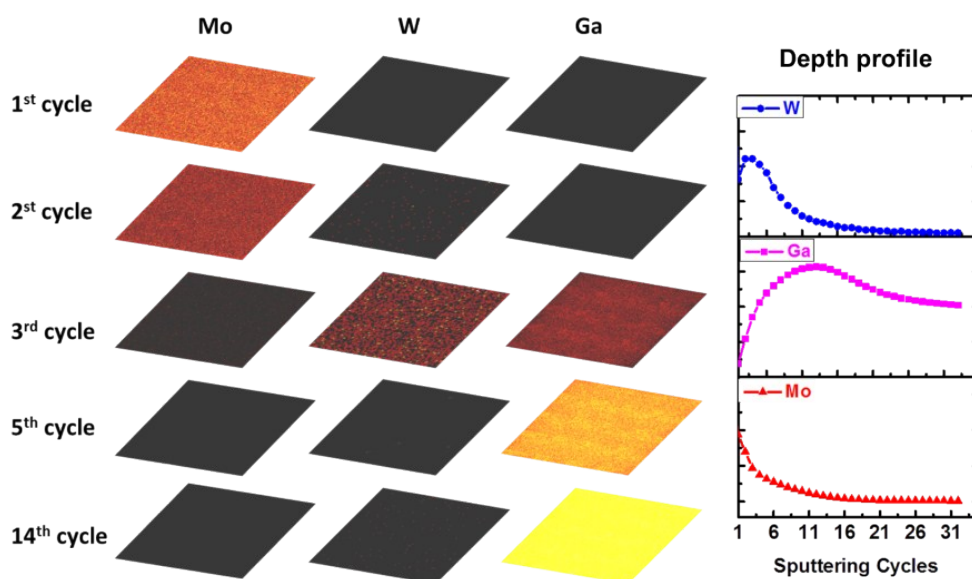


Figure S8- TOF-SIMS elemental map and depth profile of $\text{MoS}_2/\text{WSe}_2/\text{n-GaN}$.

Reference

- 1 K. Kang, S. Xie, L. Huang, Y. Han, P. Y. Huang, K. F. Mak, C.-J. Kim, D. Muller and J. Park, *Nature*, 2015, **520**, 656–660.
- 2 H. Kim, D. Ovchinnikov, D. Deiana, D. Unuchek and A. Kis, *Nano Lett.*, 2017, **17**, 5056–5063.
- 3 A. A. Pomarico, D. Huang, J. Dickinson, A. A. Baski, R. Cingolani, H. Morkoç and R. Molnar, *Appl. Phys. Lett.*, 2003, **82**, 1890–1892.
- 4 P. Deb, H. Kim, Y. Qin, R. Lahiji, M. Oliver, R. Reifenberger and T. Sands, *Nano Lett.*, 2006, **6**, 2893–2898.
- 5 F. Ahmed, M. S. Choi, X. Liu and W. J. Yoo, *Nanoscale*, 2015, **7**, 9222–9228.
- 6 H.-M. Li, D. Lee, D. Qu, X. Liu, J. Ryu, A. Seabaugh and W. J. Yoo, *Nat. Commun.*, 2015, **6**, 6564.

- 7 L. Wang, M. I. Nathan, T. H. Lim, M. A. Khan and Q. Chen, *Appl. Phys. Lett.*, 1996, **68**, 1267–1269.
- 8 H.-K. Kim, I. Adesida and T.-Y. Seong, *J. Vac. Sci. Technol. A Vacuum, Surfaces, Film.*, 2004, **22**, 1101–1104.
- 9 C. A. and E. of the L. V. III/17A-22A-41A1b, in *Group IV Elements, IV-IV and III-V Compounds. Part b - Electronic, Transport, Optical and Other Properties*, Springer-Verlag, Berlin/Heidelberg, pp. 1–14.
- 10 D. Ruzmetov, K. Zhang, G. Stan, B. Kalanyan, G. R. Bhimanapati, S. M. Eichfeld, R. A. Burke, P. B. Shah, T. P. O'Regan, F. J. Crowne, A. G. Birdwell, J. A. Robinson, A. V. Davydov and T. G. Ivanov, *ACS Nano*, 2016, **10**, 3580–3588.
- 11 R. Schlaf, O. Lang, C. Pettenkofer and W. Jaegermann, *J. Appl. Phys.*, 1999, **85**, 2732–2753.
- 12 E. W. Lee, C. H. Lee, P. K. Paul, L. Ma, W. D. McCulloch, S. Krishnamoorthy, Y. Wu, A. R. Arehart and S. Rajan, *Appl. Phys. Lett.*, 2015, **107**, 103505.
- 13 J. M. Shah, Y.-L. Li, T. Gessmann and E. F. Schubert, *J. Appl. Phys.*, 2003, **94**, 2627–2630.
- 14 W. Melitz, J. Shen, A. C. Kummel and S. Lee, *Surf. Sci. Rep.*, 2011, **66**, 1–27.
- 15 M. G. Kibria, S. Zhao, F. A. Chowdhury, Q. Wang, H. P. T. Nguyen, M. L. Trudeau, H. Guo and Z. Mi, *Nat. Commun.*, 2014, **5**, ncomms4825.
- 16 H. Henck, Z. Ben Aziza, O. Zill, D. Pierucci, C. H. Naylor, M. G. Silly, N. Gogneau, F. Oehler, S. Collin, J. Brault, F. Sirotti, F. Bertran, P. Le Fèvre, S. Berciaud, A. T. C. Johnson, E. Lhuillier, J. E. Rault and A. Ouerghi, *Phys. Rev. B*, 2017, **96**, 115312.
- 17 M. Tangi, P. Mishra, T. K. Ng, M. N. Hedhili, B. Janjua, M. S. Alias, D. H. Anjum, C. C. Tseng, Y. Shi, H. J. Joyce, L. J. Li and B. S. Ooi, *Appl. Phys. Lett.*, , DOI:10.1063/1.4959254.
- 18 M. Tangi, P. Mishra, C. C. Tseng, T. K. Ng, M. N. Hedhili, D. H. Anjum, M. S. Alias, N. Wei, L. J. Li and B. S. Ooi, *ACS Appl. Mater. Interfaces*, 2017, **9**, 9110–9117.
- 19 D. P. Gopalan, P. C. Mende, S. C. de la Barrera, S. Dhingra, J. Li, K. Zhang, N. A. Simonson, J. A. Robinson, N. Lu, Q. Wang, M. J. Kim, B. D'Urso, R. M. Feenstra, *J. Mater. Res.*, 2016, **31**, 945–958.